Atmos. Chem. Phys. Discuss., 11, 15659–15696, 2011
www.atmos-chem-phys-discuss.net/11/15659/2011/
doi:10.5194/acpd-11-15659-2011

Atmospheric Chemistry and Physics Discussions

Coastal precipitation formation and discharge based on TRMM observations

R. H. Heiblum, I. Koren, and O. Altaratz

Department of Environmental Sciences, Weizmann Institute, Rehovot, Israel

Received: 5 April 2011 – Accepted: 28 April 2011 – Published: 23 May 2011

Correspondence to: I. Koren (ilan.koren@weizmann.ac.il)

Published by Copernicus Publications on behalf of the European Geosciences Union.

Abstract

The interaction between breezes and synoptic gradient winds creates persistent convergence zones nearby coastlines. The low level convergence of moist air promotes the dynamical and microphysical processes responsible for the formation of clouds and precipitation.

Our work focuses on the winter seasons of 1998–2011 in the Eastern Mediterrenean. During the winter the Mediterrenean sea is usually warmer than the adjacent land, resulting in frequent occurence of land breeze that opposes the commom synoptic winds. Using rain-rate vertical profiles from the Tropical Rainfall Measurement Mission (TRMM) satellite, we examined the spatial and temporal distribution of average hydrometeor mass in clouds as a funtion of the distance from coastlines.

Results show that coastalines in the Eastern Mediterrenean are indeed favored areas for precipitation formation and discharge. The intra-seasonal and diurnal changes in the distribution of hydrometeor mass indicate that the land breeze is most likely the main responsible mechanism behind our results.

1 Introduction

The global hydrological cycle is of great importance to our wellbeing. Understanding this cycle is crucial when dealing with water resources management, agriculture, global demographics and politics. Precipitation processes play a key component in the hydrological cycle. Although 75 %–80 % of global precipitation occurs over oceans (see http://ww2010.atmos.uiuc.edu/(Gh)/guides/mtr/hyd/bdgt.rxml) the precipitation-evaporation budget is positive over land and negative over oceans, making precipitation our main source of fresh water. Additionally, the latent heat released in precipitation processes is a major driver of the global atmospheric circulation, and hence affects climate variations around the globe (Trenberth et al., 2009). Understanding the dynamic and microphysical processes behind precipitation formation is of great importance in semi-arid

ACPD
11, 15659–15696, 2011

climate regions which are especially sensitive to rainfall variations, such as the Eastern Mediterranean (EM), South Western US and Eastern Africa. Moreover, due to their highly non-linear nature, precipitation processes (especially cold rain processes) are still far from being resolved and our current understanding is limited (Levin and Cotton, 2009)

In this work we examine coastal precipitation formation and discharge from clouds, explained by land breezes as major contributors for mesoscale convergence, in both meteorological and climatological time scales.

1.1 Previous studies

Sea breeze (SB) and Land breeze (LB) are basically the same physical effect but with opposite temperature gradients (Schmidt, 1947; Fisher, 1960, 1961). In the SB case, a local cool and dense air mass forms over a water body, and creates a flow towards the hotter, lighter inland air mass. The LB is exactly opposite, with the denser, cooler air originating over land.The SB and LB breezes are confined mainly up to heights of 1–1.5 km, which corresponds to the boundary layer of the atmosphere. An analytical analysis (Schmidt, 1947) showed the thermally induced SB to be a stronger effect than LB, but this of course depends on local, low level temperature distributions over sea and land during day and night, and may vary from one location to another. Moreover, for both SB and LB, the vertical profiles of horizontal winds contain an upper level return flow opposed to the low level flow as expected from continuity considerations.

Interaction between breezes and synoptic gradient winds can contribute to low level convergence, and therefore to cloud and precipitation formation. Intergrating the mass conservation equation for incompressible fluids with respect to height, we get:

$$w(D) = -\int_0^D \left(\frac{\partial u}{\partial x} + \frac{\partial v}{\partial y}\right) dz \quad (1)$$

Where w is the updraft vertical velocity, u is the zonal velocity, v is the meridonial velocity and D is an arbitrary height that can be taken to be the top of the planetary

ACPD
11, 15659–15696, 2011

boundary layer. Hence, horizontal convergence of low level winds in the boundary layer result in upward vertical transport (updrafts) of mass and momentum at the top of the layer. In the common case of which the level of free convection (LFC) is above a low level inversion layer (i.e. conditional instability), these updrafts can break through the inversion, supplying heat and moisture to the upper atmosphere. Furthermore, updraft velocities are proportional to condensation rate of cloud droplets (release of latent heat) and maximum supersaturation, promoting convection processes in the cloud. In convective clouds for instance, updraft velocities are proportional to supersaturation by the relation (Fukuta, 1993):

$$(S-1) \propto w^{\frac{3}{4}} \tag{2}$$

Where $(S-1)$ is the maximum supersaturation in the cloud and w is the updraft vertical velocity. The power $\frac{3}{4}$ is derived analytically by considering the minimal time it would take a cloud to reach the maximum supersaturation ($t \propto w^{-\frac{1}{4}}$) and assuming a balance between dry adiabatic supersaturation generation ($\propto w$) and droplet diffusional growth ($\propto \frac{S-1}{t}$). Theory and simulations show that higher supersaturation/updrafts can increase both diffusional growth rates and coalescence of droplets (Mordy, 1959; Leighton and Rogers, 1974; Rogers and Yau, 1989; Nelson, 1971), which are crucial in the initiation and growth of warm precipitation (involves only liquid water). This is also pronounced in mixed phased clouds, where the supersaturation of vapor relative to ice is much higher than relative to water, and diffusional ice growth is more rapid (Stickley, 1940; Byers, 1965). Additionally, stronger updrafts transport more droplets above the freezing level of the cloud, promoting the highly efficient accretion/riming (i.e. growth by coalesence of ice particles and supercooled droplets) processes that initiate cold rain (Houghton, 1950, 1968; Ludlam, 1952; Hindman and Johnson, 1972; Reinking, 1975).

ACPD
11, 15659–15696, 2011

Observations indeed show that low level convergance promotes cloud convection. Frequent nocturnal thunderstorms (Neumann, 1951) observed near the Eastern Mediterranean coastline were explained by: (i) the convergence of synoptic gradient winds with LB (ii) the convergent effect coastline curvature may play on low level winds, with concave coastlines favoring LB convergence and convex coastlines favoring SB convergence. Similar effects of cloud formation as a result of low level convergence were observed (Purdom, 1976) nearby other land-water interfaces such as rivers and lakes. Furthermore, breeze fronts were seen to interact with preexisting convection lines and thunderstorms, greatly intensifying the mesoscale convection. Radar observations of LBs opposing gradient winds (Meyer, 1971; Schoenberger, 1984) showed frontal zones of nocturnal cumulus form nearby coastlines and propagate further offshore at a speed dependent on the temperature difference between the land and sea. These LB fronts usually dissipated after sunrise (i.e. land heating) and were most pronounced when the gradient winds and the LB were of comparable magnitudes. An example for such a LB front is shown in Fig. 1, where a nearly stationary line of precipitating clouds formed off the coast of Israel.

Observations (Atkins and Wakimoto, 1997) and numerical studies (Baker et al., 2001; Nicholls et al., 1991) over the Florida Peninsula put emphasis on the importance of converging synoptic gradient winds and SB. The convergence was seen to induce vertical heat and moisture fluxes, initiating moist deep convection processes and later on precipitation in the peninsula. Non-linear interactions between the factors above, soil moisture and coastline curvature may determine the locations of intense precipitation (Baker et al., 2001). Additional numerical studies of coastline effects are presented in the Sect. 1.2.

As follows from the thermally driven nature of breezes, their effects are expected to have significant diurnal variability. Java Island in the SE pacific is an extreme case for a breeze dominated diurnal precipitation regime (Qian, 2008). The Island is surrounded with warm waters and experiences daytime (nighttime) precipitation concentrated over the land (sea). The high mountain range along the Island's interior produces daytime

ACPD
11, 15659–15696, 2011

(nighttime) anabatic (katabatic) winds that flow in phase with the local breeze, intensifying the diurnal cycle.

Orographic forcing, also discussed in this work, is considered to be another strong influence on cloud and precipitation formation (Smith, 1989, 2006; Houze, 1993). Horizontal moist winds that approach a topographic obstacle are forced to rise and cool with a vertical velocity proportional to the horizontal wind velocity and obstacle height gradient. The forced updrafts induce the formation of clouds and precipitation as discussed above. The location of maximum precipitation with respect to the obstacle depends mainly on the ratio between the microphysical processes and advection time scales, and can range from 50 km upwind (e.g. with very weak horizontal winds of $\sim 2\,m\,s^{-1}$) the peak height location to slightly downwind (Pathirana et al., 2005). Moreover, gravity wave dynamics may create an upwind tilt in the condensation pattern. Generally, most of the precipitation falls on the upslope of the obstacle, with a maximum near its peak. The flow reaching the lee-side receives little precipitation due to adiabatic descent (warming) and depletion of moisture. In the case of an unstable, convective atmosphere, topographic obstacles are considered especially efficient in depleting the cloud's water content.

In some cases, orographic forcing near coastal areas may combine with local mesoscale breezes and create a coupled effect. A previous study in central Israel (Rosenfeld, 1986) concluded that clouds "feel" the presence of an orographic obstacle 15 km upwind the mean flow, not far from the coastlines.

1.2 Eastern mediterranean

The last IPCC report (Climate Change 2007 Synthesis report, Sects. 3.2, 3.3. Available at: http://www.ipcc.ch/) predicts that the Mediterranean region will experience a hotter and drier climate, among others due to the predicted expansion of the Hadley circulation derived from global warming (Lu et al., 2007). Such climate changes may have devastating implications on water resources for the already water stressed countries in the region. According to Köppen's climate classification (Goldreich, 2003),

ACPD
11, 15659–15696, 2011

Mediterranean climates are characterized by hot, dry summers and cold, wet winters with most of the rainfall concentrated in the months D-J-F.

During the Northern Hemisphere winter, the southward drift of the subtropical high enables cold air from Europe to penetrate into the Mediterranean where cold low pressure systems are formed (Alpert et al., 1990a, b). These systems may further intensify through processes of low-level baroclinic instability i.e. large thermal contrast between the sea and cold air above and lee cyclogenesis near southern Turkey. Some of these cyclones reach the EM and are called Cyprus lows, acquiring their name from their mean geographic location. The passage of a Cyprus low is dominated by westerly winds along the central part of the Eastern Mediterranean coast (Zangvil and Druian, 1990) and constitutes as the most common synoptic setting under which precipitation develops in the EM, yielding about 95 % of the rainfall in the central and northern parts of Israel (Goldreich, 2003). The common setting of a Cyprus low is shown in Fig. 2, from which it can be seen that the gradients winds tend to flow inland except near western Turkey. Another type of synoptic system that can produce precipitation in the eastern Mediterranean is the "Red Sea Trough". It will not be discussed hereafter due to very low rainfall related to these systems.

During the winter months (November–March), EM Sea Surface temperatures are usually warmer than the adjacent land by 2–10 °C, making LB a common phenomena during the winter (Neumann, 1951; Goldreich, 2003; Levy et al., 2008). The LB magnitude varies both diurnally: maximum (minimum) Land-Sea Temperature Difference (LSTD) at sunrise (afternoon), and seasonally: maximum (minimum) LSTD during December (March). The cyclones reaching the EM also display significant intra-seasonal variability (Goldreich et al., 2004, 2006; Alpert et al., 1990b). November and December are considered transition months from autumn to winter and experience relatively shallow upper level troughs and weak (shallower) vortices. On the other hand, the period of January till March is considered "classic" winter, with deep upper level troughs and intense vortices. The EM may be a classic case where the interaction between LB and synoptic winds promotes convection and precipitation formation, because most of

ACPD
11, 15659–15696, 2011

the rain in the region is attributed to frontal and post frontal convective clouds. Typically during the winter season in Israel, rain only forms in clouds that reach a minimum height of 3 km (around −5 °C). Rain clouds often develop vertically to heights higher than 5 km (−20 °C), making cold rain the dominant precipitation process (Rosenfeld, 1986). An area of low level convergence with high updrafts over the Mediterranean Sea would be favorable for cloud and precipitation formation by supplying moisture to the mid-atmosphere and speeding up mixed phase and cold rain processes (see Sect. 1.1). Ground based radar observations near the Israeli coastline show a 1:1 to 3:1 sea to land rainfall ratio during winters (Levin et al., 2004), with the ratio peak in November, suggesting a stronger contribution of LB in the early stages of winter. Further evidence for LB effect is manifested through diurnal variation of lightning activity (Altaratz et al., 2003), showing a clear maximum of flashes over sea (land) during midnight (afternoon). A similar trend exists for the diurnal variability of rain rates (Kutiel and Sharon, 1980), with inland precipitation peaking afternoon, and coastal precipitation peaking around midnight with a second peak around noon.

The interaction between westerly gradient winds and land breeze was studied using a 2-D non-Hydrostatic numerical simulation (Khain et al., 1993). They conclude that this interaction is the main cause for precipitation in the model. The magnitude of background gradient winds and LSTD directly affect the intensity and location of precipitation with respect to the coastline. As would be expected, stronger gradient winds shift precipitation towards inland and larger LSTD shifts precipitation towards the sea. Furthermore, a convective convergence zone located *offshore*, coupled with precipitation downdrafts of cold air located slightly *onshore*, may result in positive feedback and enhancement of the land breeze circulation. This feedback was shown to be crucial in sustaining the breeze circulation (Khain and Sednev, 1996; Khain et al., 1996). The optimal values of precipitation yield over land occur when the convergence zone is located 10–20 km offshore. It is important to note that topography was excluded from the model.

ACPD
11, 15659–15696, 2011

In this work we perform a long term study of precipitation in the coastal region, both spatially and temporally. More than 13 yr of high resolution space-borne radar data collected by the Tropical Rain Measurement Mission (TRMM) satellite are used. Furthermore, the coastline mesoscale dynamics effect on the precipitation is separated from the orographic forcing. Section 2 discusses the methods used to retrieve and analyze the observational data. In Sect. 3 the results of the study are presented and in Sect. 4 we discuss the results in light of physical mechanisms reviewed in previous works and other dynamical theories.

2 Methods

High resolution precipitation data ($\sim 5 \times 5\,km^2$ footprint) was acquired from NASA's Tropical Rainfall Measurement Mission (TRMM) database (for data see: http://mirador.gsfc.nasa.gov). TRMM satellite has been in orbit since 1997 and is equipped with both active and passive remote sensing instruments. Its main advantage compared to other precipitation measuring satellites is the first of a kind 13.8 GHz precipitation radar installed onboard, which enables us to obtain high resolution vertical profiles (250 m) of precipitation. TRMM spatially covers 35° N to 35° S in a non-sun-synchronous orbit, providing complete temporal statistics for the tropics and sub-tropical regions.

2.1 TRMM 2B31

The TRMM product used in this work was the level 2 combined 2B31 product (Haddad et al., 1997; Kummerow et al., 2000). 2B31 combines both precipitation radar (PR) and Thermal Microwave Imager (TMI) data to obtain the precipitation vertical profile estimation. The product output is adapted to the PR vertical profile with a ~5 km footprint (~4 km before August 2001). The total swath is 250 km and the vertical profile ranges from the surface up to 20 km above the earth's ellipsoid, with a resolution of 250 m (i.e. total of 80 vertical levels). The algorithm is based on comparing the total

ACPD
11, 15659–15696, 2011

integrated column attenuations given by the PR and TMI, in order to reduce the uncertainty of the a prioi selected drops size distribution (DSD) for the PR algorithm. The combined approach gives importance to the PR and TMI as their ambiguities warrant. The fine resolution of the PR is expected to compensate for the ambiguity of the TMI (e.g. detecting freezing levels and vertical distribution) and the robustness of the TMI should reduce errors made by the radar when integrating quantities (PR is very sensitive to hydrometeor size). Due to the wavelength of the PR, 2B31 is inherently less sensitive to weak rain and drizzle ($<0.7\,\mathrm{mm\,hr^{-1}}$) which are common in cases of certain stratiform clouds. Like all passive microwave imagers, the TMI performs best over homogeneous water bodies. Hence, over land the algorithm is dominated by PR measurements (Adler et al., 2009). For more on the algorithm see references (Haddad et al., 1997; Iguchi et al., 2000).

Many validation studies have been conducted for the PR, TMI and combined level 2 products. Validation results vary on spatial and seasonal temporal scales (Wolff et al., 2005; Adeyewa and Nakamura, 2003), showing weaker performance in estimating accumulated rainfall compared to lower resolution, rain-gauge calibrated TRMM products such as the 3B42 (Adeyewa and Nakamura, 2003; Nicholson et al., 2003; Kummerow et al., 2000). Nevertheless, the products have successfully been able to capture diurnal precipitation and climatological trends (Yang and Smith, 2006; Shin et al., 2000). Moreover, the combined 2B31 product tends to give improved results and lower biases compared to the PR and TMI products alone (Masunaga et al., 2002; Wolff et al., 2005; Wolff and Fisher, 2008), especially at marine and coastal areas.

2.2 Region of interest and distance from coastlines

We focus the study on the East Mediterranean (EM), the region of interest (ROI) spans from 30° N–36° N (TRMM's northern limit) and 30° E–38° E (see Fig. 3). 2B31 data was collected for 13 winter seasons (November–March) from 1998 till 2011. The data was spatially sorted into a 5 km × 5 km uniform grid that corresponds best to TRMM level 2 data. High resolution (2 min of a degree ~=3.5 km) coastline and topography data was

ACPD
11, 15659–15696, 2011

taken from NCEP/NCAR (see: http://dss.ucar.edu/datasets/), and linearly interpolated to fit the ROI grid. Using all datasets, we sorted the TRMM data as function of distance to the nearest coastline (i.e. the normal from the coastline to each grid pixel). All results in this work are displayed with respect to distance from the nearest coastline, with positive (negative) distances corresponding to rain over land (sea). The error was taken to be ±7 km, which is the diagonal between two pixels.

Two additional sub-regions were defined in order to focus on orographic effects nearby coastal areas (see Fig. 3). One named "Lebanon" and corresponds to the Lebanese region which is characterized by two extreme high mountain ridges, one of them located in close proximity to the coastline. The first ridge (referred to as Mount Lebanon ridge) peaks around 20–25 km inland, followed by successive second ridge (referred to as Anti-Lebanon ridge) located 60 km inland. Both Lebanon ridges are of comparable heights (average of ∼1.5 km), and are separated by a high elevation plateau. The second sub-region named "Israel", and corresponds to the central part of Israel. This sub-region consists of two high mountain ridges as well, although not as steep as in Lebanon and not located as close to the coastline. The first mountain ridge (referred to as Judea ridge) reaches its highest elevation (average of ∼600 m) 45–50 km inland. Judea ridge is followed by a sharp drop in elevation down to the Jordan Valley and a rapid rise afterwards to the second mountain ridge (referred to as Jordan ridge). Jordan ridge reaches its highest elevation (average of ∼700 m) 100–110 km inland. The distinct differences (i.e. ridges' height and proximity to coastlines) between both sub-regions may help us better estimate the role orographic forcing has on precipitation processes compared to other precipitation promoting dynamical effects.

2.3 Precipitation mass

Vertical profiles of rain rates [mm hr^{-1}] were translated in this study into column Integrated Hydrometeor Mass (IHM, [kg m^{-2}]) with the use of the drops size distribution (DSD) parameter in the 2B31 product (Haddad et al., 1997). Integrated Hydrometeor Mass (IHM) was taken for several reasons. First, using information from all vertical

ACPD
11, 15659–15696, 2011

levels allows more robust analysis of larger statistics compared to if only one vertical level was considered. Second, we get a measure of the total amount of hydrometeors formed throughout the vertical profile. Finally, using integrated mass minimizes data variability in comparison to other parameters, such as surface rain rate or maximum rain rate in the column. IHM values in this work are not normalized by the number of rain days, and can not be considered an accurate measure for accumulated rain at the surface. Nevertheless, we found that IHM and simultaneous surface rain rate are linearly correlated with $R^2 = 0.806$, and therefore can assume that IHM is proportional to rain rates at the surface.

2.4 Intra-seasonal variability

From reasons discussed above (see Sect. 1.2), we divided the data analysis to two sub-seasons, one autumnal (November–December) and one wintery (January–March). Preliminary analysis of the data confirmed that there indeed is a distinct difference in IHM quantities and spatial distribution between the two sub-seasons. Moreover, we analyzed EM 850 hPa wind and 500–1000 hPa layer thickness data from NCEP reanalysis (see: http://www.esrl.noaa.gov/psd/data/gridded/) which correspond to the rain events during the study time span. The wind average increases during the winter season, from 5.1 [m s^{-1}] during November–December, to 6.8 [m s^{-1}] during January–March, further indicating that pressure systems in the EM are more intense during the second part of winter. The 500–1000 mb thickness is proportional to the average virtual temperature between the two pressure levels i.e. Hypsometric equation (Wallace and Hobbs, 2006a). The average thickness decreases from 5607 [m] during November–December to 5550 [m] during January–March, indicating that the atmosphere is cooler during the January–March sub-season.

ACPD
11, 15659–15696, 2011

3 Results

Figure 4 shows the IHM average per grid pixel for the entire EM, icluding all 13 winter seasons. TRMM overpasses with no rain were not included in the averaging, because we are interested in average IHM values that represent rainclouds in this region. It is important to stress that the results are not normalized by the number of counts per pixel. Hence, IHM values represent the characteristic hydrometeor profile per precipitation event and not accumulated measures such as accumulated rain.

A band of high IHM relative to the rest of the domain clearly follows the coastlines, and appears to be centered slightly offshore. The band represents an area of enhanced precipitation formation, with vertically developed clouds and high rain rates throughout the vertical profile. Pixels with extremely high IHM ($>0.8\,\mathrm{kg\,m^{-2}}$) at the south eastern part of the domain should be neglected due to poor statistics. We can explain the highlighted band of IHM distribution in Fig. 4 by two main dynamical mechanisms. The convergence of LB and gradient winds, and orographic lifting. The proximity of mountains to the coastlines in some parts of the domain might imply that the band is of orographic nature, however, the band exists near flat terrain (e.g. southern part of the EM and parts of the Cyprus Island) coastal regions as well, favoring a land-sea difference mechanism. Hence, further analysis is needed to differentiate between the two mechanisms. In the next sections we shall focus on the spatial and temporal patterns of IHM in the EM and its sub-regions.

3.1 Eastern mediterranean

Mean IHM (Integrated Hydrometeor Mass) as a function of the distance to the coastlines for the whole EM region is shown in Fig. 5. It is apparent that the highlighted IHM band effect (as shown in Fig. 4) is distributed like a Gaussian, and centered slightly offshore. Therefore, after the data was sorted with respect to distance from the nearest coastline (into 30 bins), a Gaussian fit was applied and is used as an objective tool to determine the IHM peak characteristics. The fit is in the form of Eq. (3):

ACPD
11, 15659–15696, 2011

$$\mathrm{fit}(x) = a \cdot e^{-\left(\frac{\mu - x}{\sigma}\right)^2} + b \quad (3)$$

Where x is the distance from the nearest coastline. The fitted Gaussian mean (μ) is used to describe the location of the effect with respect to the coastlines, standard deviation (σ) to describe the spatial extent of the effect, amplitude (a) to describe the magnitude of the dynamical effect, and baseline (b) to describe the background IHM values far from the coastlines. Gaussian main peak height (see Fig. 5) is the highest IHM value reached by the fitting curve.

There are pronounced intra-seasonal differences which emphasize the argument that IHM values represent the characteristic precipitation profile and not accumulated rainfall. Taking the coastal cities of Tel-Aviv (Israel), Larnaka (Cyprus), and Lattakia (Syria) as representing examples, accumulated rainfall increases from 205, 128, 255 mm during November–December to 276, 165, 351 mm during January–March (data taken from the World Meteorological Organization (WMO) website, http://worldweather.wmo.int), an increase of 34 %, 28 %, and 37 %, respectively. This is in contrary to IHM values in the EM, for which the November–December peak is $\sim 0.50\,\mathrm{kg\,m^{-2}}$ compared to $\sim 0.35\,\mathrm{kg\,m^{-2}}$ for January–March, a decrease of more than 30 %. Lower temperatures which imply reduced liquid water content (LWC) in the second part of the winter can partly explain this. Along with that, the peak height relative to the baseline IHM is slightly higher in November–December ($0.25\,\mathrm{kg\,m^{-2}}$) compared to January–March ($0.2\,\mathrm{kg\,m^{-2}}$). The mean (standard deviation) of the November–December Gaussian is -9 ± 7 (37) km, whereas for January–March we get -3 ± 7 (40) km. It is apparent that peaks for both sub-seasons are located offshore, suggesting that most of the precipitation in the EM forms over the sea.

The method of single Gaussian fitting as done for the whole EM does not describe well some important features in the data, such as the double peak in November–December and the large right tail of the January–March Gaussian, resulting in an underestimation of the January–March STD. Since the whole EM IHM data is included in this analysis, it is influenced by many local effects together (e.g. orographic and surface

ACPD
11, 15659–15696, 2011

friction effects), which cannot be decoupled. For this purpose we shall examine two sub-regions separately, Lebanon and Israel.

3.2 Lebanon

As seen above, it is necessary to analyze smaller regions of well specified topography in order to decouple the orographic and LB effects on precipitation formation. The spatial distribution of the IHM in "Lebanon" sub-region (see Fig. 3) is shown in Fig. 6. We assume the distribution is a simplified superposition of two Gaussians (i.e. we add another Gaussian term to Eq. 3), one most likely related to the convergence of LB and gradient winds (LB peak), and the other related to orographic lifting (orographic peak). The average topography profile as a function of the distance from the coast is displayed in Fig. 6 as well. The results for November–December show that the two Gaussian assumption fits the data with high correlation ($R^2 = 0.94$). Fitting analysis reveals that the LB:orographic amplitude Gaussian ratio is 2:1, with a main peak height of 0.56 kg m^{-2}. The LB peak mean (standard deviation) is -22 ± 7 (22) km compared to 5 ± 7 (9) km for the orographic peak. Meaning that the LB effect dominates offshore precipitation formation and affects a larger area than the narrow orographic effect, which dominates onshore precipitation formation.

The orographic peak in hydrometeor mass is located around 20 km before the peak elevation of the Mount Lebanon ridge (located around 20–25 km from the coast), and seems to correspond to the location with the highest gradient in topography (see the green curve in Fig. 6). The third Gaussian was not applied to the third peak located at −100 km because it is probably related to coastline effects in proximity of Eastern Cyprus.

During the January–March sub-season, although not as clearly separated, two Gaussians are successfully fitted ($R^2 = 0.98$) to the sorted data curve. The fitting analysis LB:orographic amplitude ratio now 1:2, suggesting that the IHM distribution is now dominated by the orographic peak. The LB peak mean (standard deviation) shifts to -28 ± 7 (10) km compared to -8 ± 7 (33) km for the orographic peak. Although both

ACPD
11, 15659–15696, 2011

peaks' locations shift offshore compared to November–December (6 km and 13 km for the LB and orographic peaks, respectively), the weight of the distribution shifts towards the land, as indicated by the amplitude ratio and switch in standard deviation magnitudes. January–March IHM values are lower, as expected, with peak IHM value of 0.38 kg m^{-2}, and consistent with the whole EM. As previously discussed, if LB interaction with gradient winds and orographic lifting are considered to be the physical mechanism behind the highlighted IHM band, we would expect to see a diurnal pattern. Nighttime experiences the largest SST-Land temperature difference, so we would expect to see the strongest and furthest offshore IHM signal during the night. Radiative surface heating (though limited due to cloud shading) of land and mountain slopes should result in an opposite effect, with a maximum IHM signal over land during the day. To support the idea that diurnal variations are due to mesoscale dynamics and not synoptic scale forcing, we checked the diurnal variation of IHM far away from coastlines (more than 100 km offshore) and saw no clear pattern over the sea. Hence, our basic assumption is that the diurnal occurrence of EM winter storms is distributed randomly. The time evolution of the IHM distribution with respect to the coastline in Lebanon is displayed in Fig. 7. To reduce the noise, we used a moving ±3 h span average e.g. the data from 6 (Local Time) is an average of the data collected between 03:00 and 09:00 (see Fig. 7 caption for more details on diurnal analysis).

Considering the November–December sub-season, the separation to two peaks is clearly seen throughout the diurnal cycle. The offshore LB peak displays two modes of high IHM values: (i) during nighttime hours (23:00–05:00 ± 3 h) (ii) during daytime hours (12:00–18:00 ± 3 h). The latter mode does not fit the land-sea temperature difference diurnal evolution. Moreover, the distribution spreads offshore to its largest extent during daytime and not nighttime as expected. The orographic peak IHM values remain more stable throughout the diurnal cycle, showing maximum values during the nighttime (00:00–5:00 ± 3 h). Far inland IHM (>25 km) reaches its highest values during daytime hours (10:00–16:00 ± 3 h). The −100 km offshore peak which is attributed to Cyprus's coastline shows no diurnal cycle.

ACPD
11, 15659–15696, 2011

January–March shows different behavior than November–December. The separation to LB and orographic peaks is less obvious, and can only be distinguished during the morning hours. The LB and orographic peaks reach their minimum magnitude during the afternoon. Both peaks (LB and orographic) intensify during the nighttime and morning hours (00:00–12:00 ± 3 h). Compared to the "noisier" first sub-season, the total distribution is neatly confined between −50 km and 50 km throughout the day. The far inland peak disappears during late winter.

3.3 Israel

The "Israel" sub-region (see Fig. 3) spatial distribution of the IHM is shown in Fig. 8. Rainfall occurs less in this region compared to the northern Lebanon region that is closer to the cyclones' centers. This results in poorer statistics and "noisier" data. Therefore, we reduced the number of sorting bins to 25 in order to reduce fluctuations in the data. Results from Israel sub-region suggest that both Judea and Jordan mountain ridges effect the IHM distribution considerably. Hence, we used three Gaussians in the analysis: LB, Judea and Jordan (i.e. we added a third Gaussian term to Eq. 3).

Similar to Lebanon, the LB Gaussian dominates during November–December, reaching IHM = 0.52 kg m^{-2}. The LB:Judea:Jordan Gaussian fitting amplitude ratio is 5:2:4 during this sub-season. The three peaks are located at −20 ± 7 (38) km, 28 ± 7 (13) km and 75 ± 7 (14) km, the LB peak having the largest spatial extent. Fitting correlation is $R^2 = 0.93$. As seen for Lebanon, orographic peaks are located 20–30 km before the mountain ridges, and correspond to the largest topographic height gradients. Secondary peaks located farther offshore at −80 km, −120 km are "artifacts" of the curvature of the coastline towards Egypt. i.e. Israel sub-region includes LB effects of Egypt as well. The peaks appear only during the November–December sub-season, when Egypt LB is at its maximum.

Similar to Lebanon sub-region, the January–March sub-season shows less separation between Gaussians, with the LB and Judea orographic peaks nearly combining to a single peak. The three peaks are located at −28 ± 7 (21) km, 11 ± 7 (29) km and

ACPD
11, 15659–15696, 2011

78 ± 7 (24) km, with Judea orographic peak maximum IHM value of 0.37 kg m^{-2}. The LB and Judea peaks shift towards the sea by 8 km and 17 km (compared to November–December location), respectively, similar to the shift seen for the Lebanon sub-region. Jordan peak shows no change in its location. The strongest intra-seasonal change is the decrease in LB peak amplitude, reflected by the LB:Judea:Jordan amplitude ratio of 3:5:3. Furthermore, the orographic Gaussians widen considerably (~100 %), while the LB Gaussian losses ~50 % of its spatial spread.

Diurnal patterns of IHM for "Israel" sub-region are shown in Fig. 9. Contrary to Lebanon, both winter sub-seasons show a IHM diurnal cycle that partly fits the land-sea temperature difference diurnal evolution. During November–December, the peak of the IHM distribution propagates offshore as the night progresses, reaching a maximum extent around 08 : 00 ± 3 h. The offshore peak stays intact and intensifies during daytime hours (12:00–18:00 ± 3 h), exhibiting identical behavior to the Lebanon sub-region offshore peak during November–December. The Judea and Jordan orographic peaks (at ~30 km and ~80 km inland) show maximum values during the afternoon (12:00-18:00 ±3 h) as well. Secondary offshore peak at −80 km is attributed to Egypt's coastline, and not discussed here.

As seen in Fig. 8, LB and Judea orographic peak spread out and merge during January–March. The combined peak intensifies and widens during the evening and night and reaches an offshore maximum extent around 06:00–07:00 ± 3 h. During the daytime the LB peak clearly decreases while onshore IHM values dominate the distribution. The Jordan peak is weaker and reaches its maximum values and spatial spread during the morning hours (06:00–10:00 ± 3 h). A pronounced feature of both sub-seasons is the IHM local minima located at the rain shadow of the Judea ridge.

4 Summary and discussion

Precipitation data in this work is represented by Mean Integrated Hydrometeor Mass (IHM [kg m^{-2}]), which serves as a measure of the average instantaneous precipitation

ACPD
11, 15659–15696, 2011

formation throughout the atmospheric vertical column. The use of IHM is conceptually different from most precipitation studies, which focus on accumulated rainfall [mm]. Considering the inherent algorithm differences the TRMM 2B31 product has for sea versus land areas, we looked into numerous TRMM validation and algorithm studies (see Sect. 2.1) and found no apparent bias in transition between land and sea areas. Moreover, we tested 2B31 data for different regions around the globe and found no consistent bias in coastal areas. Therefore, to our current knowledge, the 2B31 product is suitable for this work.

Results from the entire EM and its sub-regions support the idea that low level convergence of LB and synoptic winds at the sea-land interfaces have a dominant affect on precipitation formation in the region. The high topographic ridges (Mount Lebanon, Judea and Jordan) in the region also affect IHM distributions. For both Israel and Lebanon sub-regions, the orographic IHM peaks are located 20–35 km before the mountain ridges' highest elevation, strengthening the assumption that the inland peaks are indeed caused by orographic forcing. The orographic peaks correspond to the largest elevation gradients, and therefore to the largest orographic forced vertical velocities (see Sect. 1.1). There was no notable effect to the Anti-Lebanon ridge (located in Lebanon sub-region, 60 km from the coast). This may be due to depletion of much of the water content (rain shadow effect) after passing the first ridge, and due to the smaller height gradient between both ridges. Values of IHM are distributed like Gaussians with respect to EM coastlines, with their means located −30 km offshore to 30 km onshore. As implied by the shape of the distributions, we fitted a Gaussian for each effect (LB, orographic) separately.

Spatially and quantitatively, LB effect on IHM distributions change considerably during the winter in both sub-regions, as can be summarized to three points: (i) Gaussian amplitudes are larger during November–December compared to January–March. (ii) The peaks are located farther offshore during January–March. (iii) January–March sub-season experiences narrower distributions (Gaussian STD values). The orographic IHM distributions generally show opposite intra-seasonal changes to that of

ACPD
11, 15659–15696, 2011

the LB peaks: (i) Amplitudes increasing from November–December to January–March. (ii) Peak locations shift towards the sea. (iii) Widening of the distributions.

Although our analysis roughly divided the IHM distributions to LB and orographic Gaussians, it is likely that the orographic tagged Gaussians (excluding the Jordan ridge Gaussian) account for a combination of orographic forcing, LB, and surface friction effects. From basic theory (Wallace and Hobbs, 2006b) we learn that the drag force is proportional to the square of the wind speed and drag coefficient C_D (C_D grows at wind speeds larger than 5 m s^{-1}). Increased surface roughness in transition from sea to land may also play a role in low level convergence near coastlines. Frictional effects seem to be much more pronounced in the IHM distributions during January–March (stronger winds result in larger drag force), when no distinct spatial separation can be made between LB and orographic effects. During November–December, the separation is clearer and therefore each Gaussian is likely attributed to a single effect. The fact that the mean locations of the Gaussians actually display an intra-seasonal shift offshore and not onshore could be the result of the arguments above. (e.g. Judea ridge peak in Israel located at 11 km during January–March may consist of both orographic effects around 30 km inland, and LB and frictional effects near the coastline. The LB peak at −28 km represents cases of strong LB development far from the coast).

The diurnal cycles of IHM distributions show differences between Israel and Lebanon sub-regions. During the whole winter season in Israel (with the exception of the afternoon hours in November–December), diurnal patterns can be described by a see-saw pattern. Evening to morning hours exhibit an offshore transition of the IHM peak, while late morning to evening hours exhibit a transition of the IHM peak towards inland. The pattern fits the diurnal evolution of strong LB at night and weak LB during the day, and the effects of inland solar heating during the day that can de-stabilize the atmospheric profile over the land (especially over mountains). It is apparent however, that the offshore LB Gaussian during November–December is highly affected from the intense afternoon offshore peak (see Fig. 9), a fact which opposes our current proposed theory. To our knowledge, the afternoon peak has not been previously reported. Lebanon

ACPD
11, 15659–15696, 2011

sub-region diurnal cycle (November–December, see Fig. 7) combined with year-by-year analysis further confirm the credibility of the diurnal pattern. Therefore, a following work is planned to look into this diurnal feature.

Excluding the November–December afternoon offshore peak discussed above, Lebanon sub-region IHM peaks intensify during the nighttime in November–December and during the late night and morning hours in January–March. The diurnal cycles for both sub-seasons could be partially explained by LB effect, however, the cycle is fundamentally different than the cycle in Israel in two ways: (i) Israel and Lebanon diurnal cycles are out of phase. (ii) Lebanon region exhibits a strong coupling between the offshore (LB) and onshore (orographic) peaks. The main differences between Israel and Lebanon sub-regions are the location and magnitude of their topographic obstacles, combined with stronger winds in Lebanon (closer to the low pressure vortex). Hence, it is likely that Lebanon's IHM diurnal pattern is dominated by interaction of synoptic winds with topography.

The results of the spatial and temporal analysis are to the most consistent with higher SST-Land temperature differences during the first part of the winter, increasing LB and "pushing" the main convergence zone further offshore while the orographic influence is rather local. During the second part of winter, deeper vortices that produce stronger synoptic winds combine with weaker LB. Consequently, the convergence zone is displaced towards the land and clouds that form over the sea are advected more efficiently inland, resulting in larger Gaussian STD values. Additionally, the stronger winds increase frictional drag and possible interactions with topographic obstacles, further favoring precipitation formation over land. These interactions could also affect the streamlines (most importantly vertical motion) of the flow upstream the ridges (Baines, 1987; Grossman and Durran, 1984; Hughes and Ofosu, 1987), an additional explanation for the intra-seasonal offshore shift of the Gaussians' mean locations. Nevertheless, for January–March we see that the "weight" of IHM distributions is concentrated more inland than for November–December.

ACPD
11, 15659–15696, 2011

Intra-seasonal decrease in baseline IHM values can be partially attributed to changes in atmospheric vapor content. Precipitable Water (The total atmospheric water vapor contained in a vertical column of unit cross-sectional area, [kg m^{-2}]) data was obtained from NOAA-NCEP Global Data Assimilation System (GDAS), for details see: (Parrish and Derber, 1992; Saha et al., 2010). Average Precipitable Water values for the EM region are 18 kg m^{-2} during November–December and 14.5 kg m^{-2} during January–March, a decrease of ∼19 %. Thus, about half of the decrease in IHM baseline values is due to lower vapor content, while the other half is due to other dynamical and meteorological intra-seasonal changes.

The question is raised whether the highlighted IHM band (see Fig. 4) reflects the average precipitation intensity at the ground? Given the persistent westerly winds, we would expect to see an inland shift of the surface rain rate distribution. With the use of the surface rain rate parameter from the 2B31 product, we repeated the analysis as done for IHM and saw no consistent shift of the Gaussian locations towards the land or sea. Moreover, by considering low end values of TRMM detectable rain rates that correspond to a minimal drop size of ∼0.7 mm (Feingold and Levin, 1986) and terminal fall speed of ∼5 m s^{-1} (Wobus et al., 1971), combined with high end values for the precipitation profile center of gravity (2.5 km) and horizontal wind speed (10 m s^{-1}), we obtain a horizontal distance shift of 5 km, exactly TRMM's footprint. Hence, even if an inland shift exists, the resolution of our dataset is too coarse to detect it.

It is interesting to see if similar effects are as dominant in other regions of the world. Southern California (Los Angeles area) was chosen as an example because of the similar synoptic setting during the winter (Conil and Hall, 2006). Similar to the EM, peak IHM values are distributed along the coastline (see Fig. 10), probably due to a combination of mesoscale breezes and orographic effects. We expect to see similar distributions in other coastal areas around the globe as well.

In this work we focused on convective precipitation processes as affected by dynamical effects of sea-land thermal differences and topographic obstacles. Other factors such as surface fluxes, surface friction and aerosols also influence the IHM distribution

ACPD
11, 15659–15696, 2011

in the EM region and require further study. One cannot but ponder on the influences anthropogenic effects (e.g. aerosol, heat island, land use effects) may have on this water depraved region. A numerical study of aerosol effect on rain delay in Israel indicates that high aerosol loading in rainclouds may successfully shift rainfall from sea to land (Noppel et al., 2010). Finally, we have shown the benefits of using TRMM in high resolution mesoscale studies.

Acknowledgements. This research was supported in part by the Israel Science Foundation (grant 1172/10) and by the Minerva Foundation (grant 780048). TRMM data provided by NASA's Goddard Earth Sciences Data and Information Services Center (GES DISC). NCEP reanalysis data and images provided by the NOAA/OAR/ESRL PSD, Boulder, Colorado, USA, from their Web site at http://www.esrl.noaa.gov/psd/. GDAS data provided by NOAA/NCEP (MODIS Ancillary Data), from their Web site at http://ladsweb.nascom.nasa.gov/.

References

Adeyewa, Z. D. and Nakamura, K.: Validation of TRMM radar rainfall data over major climatic regions in Africa, J. Appl. Meteorol., 42, 331–347, 2003.

Adler, R. F., Wang, J. J., Gu, G. J., and Huffman, G. J.: A Ten-Year Tropical Rainfall Climatology Based on a Composite of TRMM Products, J. Meteorol. Soc. Jpn., 87, 281–293, doi:10.2151/jmsj.87A.281, 2009.

Alpert, P., Neeman, B. U., and Shay-El, Y.: Climatological analysis of Mediterranean cyclone using ECMWF data, Tellus, Series A (Dynamic Meteorology and Oceanography), 42A, 65–77, 1990a.

Alpert, P., Neeman, B. U., and Shayel, Y.: Intermonthly Variability of Cyclone Track in the Mediterrenean, J. Climate, 3, 1474–1478, 1990b.

Altaratz, O., Levin, Z., Yair, Y., and Ziv, B.: Lightning activity over land and sea on the eastern coast of the Mediterranean, Mon. Weather Rev., 131, 2060–2070, 2003.

Atkins, N. T. and Wakimoto, R. M.: Influence of the synoptic-scale flow on sea breezes observed during CaPE, Mon. Weather Rev., 125, 2112–2130, 1997.

Baines, P. G.: Upstream Blocking and Airflow Over Mountains, Annu. Rev. Fluid Mech., 19, 75–95, doi:10.1146/annurev.fl.19.010187.000451, 1987.

ACPD

11, 15659–15696, 2011

Baker, R. D., Lynn, B. H., Boone, A., Tao, W. K., and Simpson, J.: The influence of soil moisture, coastline curvature, and land-breeze circulations on sea-breeze-initiated precipitation, J. Hydrometeorol., 2, 193–211, 2001.

Byers, H. R.: Identification of ice nuclei in the atmosphere, International Conference on Cloud Physics Tokyo, 126–130, 1965.

Conil, S. and Hall, A.: Local Regimes of Atmospheric Variability: A Case Study of Southern California, J. Climate, 19, 4308–4325, doi:10.1175/JCLI3837.1, 2006.

Feingold, G. and Levin, Z.: The Lognormal Fit to Raindrop Spectra from Frontal Convective Clouds in Israel, J. Climate Appl. Meteorol., 25, 1346–1363, doi:10.1175/1520-0450(1986)025<1346:TLFTRS>2.0.CO;2, 1986.

Fisher, E. L.: An Observational Study of the Sea Breeze, J. Meteorol., 17, 645–660, 1960.

Fisher, E. L.: A Theoretical Study of the Sea Breeze, J. Meteorol., 18, 216–233, 1961.

Fukuta, N.: Water supersaturation in convective clouds, Atmospheric Research, 30, 105–126, doi:10.1016/0169-8095(93)90043-n, 1993.

Goldreich, Y.: The Climate of Israel: Observation, Research and Application, Kluwer Academic/Plenum Publishers, 2003.

Goldreich, Y., Mozes, H., and Rosenfeld, D.: Radar analysis of cloud systems and their rainfall yield, in Israel, Israel J. Earth Sci., 53, 63–76, 2004.

Goldreich, Y., Mozes, H., and Rosenfeld, D.: Analysis of rainy cloud systems by radar and satellite images in , inter-monthly variations., Merhavim (in Hebrew, Abstr), 385–396, 2006.

Grossman, R. L. and Durran, D. R.: Interaction of Low-Level Flow with the Western Ghat Mountains and Offshore Convection in the Summer Monsoon, Mon. Weather Rev., 112, 652–672, doi:10.1175/1520-0493(1984)112<0652:IOLLFW>2.0.CO;2, 1984.

Haddad, Z. S., Smith, E. A., Kummerow, C. D., Iguchi, T., Farrar, M. R., Durden, S. L., Alves, M., and Olson, W. S.: The TRMM 'day-1' radar/radiometer combined rain-profiling algorithm, J. Meteorol. Soc. Jpn., 75, 799–809, 1997.

Hindman, E. E. and Johnson, D. B.: Numerical Simulation of Ice Particle Growth in a Cloud of Supercooled Water Droplets, J. Atmos. Sci., 29, 1313–1321, doi:10.1175/1520-0469(1972)029<1313:NSOIPG>2.0.CO;2, 1972.

Houghton, H. G.: A Preliminary Quantitative Analysis of Precipitation Mechanisms, J. Meteorol., 7, 363–369, 1950.

Houghton, H. G.: On Precipitation Mechanisms and their Artificial Modification, J. Appl. Meteorol., 7, 851–859, doi:10.1175/1520-0450(1968)007<0851:OPMATA>2.0.CO;2, 1968.

ACPD

11, 15659–15696, 2011

Houze, R. A. Jr.: Orographic Clouds, in: Cloud Dynamics, Academic Press, Inc., 502–538, 1993.
Hughes, R. L. and Ofosu, K. N.: Froude number effects on flow over topography, Geophys. Astro. Fluid, 38, 177–191, 1987.
Iguchi, T., Kozu, T., Meneghini, R., Awaka, J., and Okamoto, K.: Rain-profiling algorithm for the TRMM precipitation radar, J. Appl. Meteorol., 39, 2038–2052, 2000.
Khain, A. P., Rosenveld, D., and Sednev, I.: Coastal effects in the Eastern Mediterranean as seen from experiments using a cloud ensemble model with detailed description of warm and ice microphysical processes, Atmos. Res., 30, 295–319, 1993.
Khain, A. P. and Sednev, I.: Simulation of precipitation formation in the Eastern Mediterranean coastal zone using a spectral microphysics cloud ensemble model, Atmos. Res., 43, 77–110, 1996.
Khain, A. P., Sednev, I., and Khvorostyanov, V.: Simulation of coastal circulation in the Eastern Mediterranean using a spectral microphysics cloud ensemble model, J. Climate, 9, 3298–3316, 1996.
Kummerow, C., Simpson, J., Thiele, O., Barnes, W., Chang, A. T. C., Stocker, E., Adler, R. F., Hou, A., Kakar, R., Wentz, F., Ashcroft, P., Kozu, T., Hong, Y., Okamoto, K., Iguchi, T., Kuroiwa, H., Im, E., Haddad, Z., Huffman, G., Ferrier, B., Olson, W. S., Zipser, E., Smith, E. A., Wilheit, T. T., North, G., Krishnamurti, T., and Nakamura, K.: The status of the Tropical Rainfall Measuring Mission (TRMM) after two years in orbit, J. Appl. Meteorol., 39, 1965–1982, 2000.
Kutiel, H. and Sharon, D.: Diurnal-Variation of Rainfall in Israel, Archiv Fur Meteorologie Geophysik Und Bioklimatologie Serie a-Meteorologie Und Geophysik, 29, 387–395, 1980.
Leighton, H. G. and Rogers, R. R.: Droplet Growth by Condensation and Coalescence in a Strong Updraft, J. Atmos. Sci., 31, 271–279, doi:10.1175/1520-0469(1974)031<0271:DGBCAC>2.0.CO;2, 1974.
Levin, Z., Breitgang, J., and Shtivelman, D.: Precipitation over the sea in the coastal area of Israel: a possible new source of water, 14th International Conference on Clouds and Precipitation, 1228–1231, 2004.
Levin, Z. and Cotton, W. R.: Aerosol Pollution Impact on Precipitation: A Scientific Review, Springer, 2009.
Levy, I., Dayan, U., and Mahrer, Y.: A five-year study of coastal recirculation and its effect on air pollutants over the East Mediterranean region, J. Geophys. Res., 113, D16121,

ACPD
11, 15659–15696, 2011

doi:10.1029/2007JD009529, 2008.
Lu, J., Vecchi, G. A., and Reichler, T.: Expansion of the Hadley cell under global warming, Geophys. Res. Lett., 34, L06805, doi:10.1029/2006gl028443, 2007.
Ludlam, F. H.: The production of showers by the growth of ice particles, Q. J. Roy. Meteor. Soc., 78, 543–553, doi:10.1002/qj.49707833805, 1952.
Masunaga, H., Iguchi, T., Oki, R., and Kachi, M.: Comparison of rainfall products derived from TRMM microwave imager and precipitation radar, J. Appl. Meteorol., 41, 849–862, 2002.
Meyer, J. H.: Radar Observations of Land Breeze Fronts, J. Appl. Meteorol., 10, 1224–1232, doi:10.1175/1520-0450(1971)010<1224:ROOLBF>2.0.CO;2, 1971.
Mordy, W.: Computations of the Growth by Condensation of a Population of Cloud Droplets, Tellus, 11, 16–44, 1959.
Nelson, L. D.: A Numerical Study on the Initiation of Warm Rain, J. Atmos. Sci., 28, 752–762, 1971.
Neumann, J.: Land Breezes and Nocturnal Thunderstorms, J. Meteorol., 8, 60–67, 1951.
Nicholls, M. E., Pielke, R. A., and Cotton, W. R.: A 2-Dimensional Numerical Investigation of the Interaction between Sea Breezes and Deep Convection over the Florida Peninsula, Mon. Weather Rev., 119, 298–323, 1991.
Nicholson, S. E., Some, B., McCollum, J., Nelkin, E., Klotter, D., Berte, Y., Diallo, B. M., Gaye, I., Kpabeba, G., Ndiaye, O., Noukpozounkou, J. N., Tanu, M. M., Thiam, A., Toure, A. A., and Traore, A. K.: Validation of TRMM and other rainfall estimates with a high-density gauge dataset for West Africa. Part II: Validation of TRMM rainfall products, J. Appl. Meteorol., 42, 1355–1368, 2003.
Noppel, H., Pokrovsky, A., Lynn, B., Khain, A. P., and Beheng, K. D.: A spatial shift of precipitation from the sea to the land caused by introducing submicron soluble aerosols: Numerical modeling, J. Geophys. Res., 115, D18212, doi:10.1029/2009jd012645, 2010.
Parrish, D. F. and Derber, J. C.: The National Meteorological Center's Spectral Statistical-Interpolation Analysis System, Mon. Weather Rev., 120, 1747–1763, 1992.
Pathirana, A., Herath, S., and Yamada, T.: Simulating orographic rainfall with a limited-area, non-hydrostatic atmospheric model under idealized forcing, Atmos. Chem. Phys., 5, 215–226, doi:10.5194/acp-5-215-2005, 2005.
Purdom, J. F. W.: Some Uses of High-Resolution GOES Imagery in Mesoscale Forecasting of Convection and its Behavior, Mon.Weather Rev., 104, 1474–1483, 1976.
Qian, J.-H.: Why Precipitation Is Mostly Concentrated over Islands in the Maritime Continent,

ACPD
11, 15659–15696, 2011

J. Atmos. Sci., 65, 1428–1441, doi:10.1175/2007jas2422.1, 2008.
Reinking, R. F.: Formation of Graupel, J. Appl. Meteorol., 14, 745–754, doi:10.1175/1520-0450(1975)014<0745:FOG>2.0.CO;2, 1975.
Rogers, R. R., and Yau, M. K.: Short Course In Cloud Physics, Third ed., Butterworth-Heinmann, 1989.
Rosenfeld, D.: Dynamic Characteristics of Cumuliform Clouds and Cloud Systems and their Influence on Rainfall, Ph.D., Atmos. Sci., Hebrew University, Jerusalem, 1986.
Saha, S., Moorthi, S., Pan, H.-L., Wu, X., Wang, J., Nadiga, S., Tripp, P., Kistler, R., Woollen, J., Behringer, D., Liu, H., Stokes, D., Grumbine, R., Gayno, G., Wang, J., Hou, Y.-T., Chuang, H.-Y., Juang, H.-M. H., Sela, J., Iredell, M., Treadon, R., Kleist, D., Van Delst, P., Keyser, D., Derber, J., Ek, M., Meng, J., Wei, H., Yang, R., Lord, S., Van Den Dool, H., Kumar, A., Wang, W., Long, C., Chelliah, M., Xue, Y., Huang, B., Schemm, J.-K., Ebisuzaki, W., Lin, R., Xie, P., Chen, M., Zhou, S., Higgins, W., Zou, C.-Z., Liu, Q., Chen, Y., Han, Y., Cucurull, L., Reynolds, R. W., Rutledge, G., and Goldberg, M.: The NCEP Climate Forecast System Reanalysis, B. Am. Meteorol. Soc., 91, 1015–1057, doi:10.1175/2010BAMS3001.1, 2010.
Schmidt, F. H.: An Elementary Theory of the Land and Sea Breeze Circulation, J. Meteorol., 4, 9–20, doi:10.1175/1520-0469(1947)004<0009:AETOTL>2.0.CO;2, 1947.
Schoenberger, L. M.: Doppler Radar Observation of a Land-Breeze Cold-Front, Mont. Weather Rev., 112, 2455–2464, 1984.
Shin, D. B., North, G. R., and Bowman, K. P.: A summary of reflectivity profiles from the first year of TRMM radar data, J. Climate, 13, 4072–4086, 2000.
Smith, R. B.: Mechanisms of Orographic Precipitation, Meteorological Magazine, 118, 85–88, 1989.
Smith, R. B.: Progress on the theory of orographic precipitation, Geological Society of America, Boulder, Colorado, 2006.
Stickley, A. R.: An Evaluation of the Bergeron-Findeisen Precipitation Theory, Mon. Weather Rev., 68, 272–280, doi:10.1175/1520-0493(1940)068<0272:AEOTBP>2.0.CO;2, 1940.
Trenberth, K. E., Fasullo, J. T., and Kiehl, J.: Earth's Global Energy Budget, B. Am. Meteorol. Soc., 90, 311–323, doi:10.1175/2008BAMS2634.1, 2009.
Wallace, J. M., and Hobbs, P. V.: Atmospheric Science, 2nd ed., 70 pp., 2006a.
Wallace, J. M., and Hobbs, P. V.: Atmospheric Science, 2nd ed., 383–391, 2006b.
Wobus, H. B., Murray, F. W., and Koenig, L. R.: Calculation of the Terminal Velocity of Water Drops, Journal of Applied Meteorology, 10, 751–754, doi:10.1175/1520-

ACPD
11, 15659–15696, 2011

0450(1971)010<0751:COTTVO>2.0.CO;2, 1971.
Wolff, D. B., Marks, D. A., Amitai, E., Silberstein, D. S., Fisher, B. L., Tokay, A., Wang, J., and Pippitt, J. L.: Ground Validation for the Tropical Rainfall Measuring Mission (TRMM), J. Atmos. Ocean. Tech., 22, 365–380, 2005.
Yang, S. and Smith, E. A.: Mechanisms for diurnal variability of global tropical rainfall observed from TRMM, J. Climate, 19, 5190–5226, 2006.
Zangvil, A. and Druian, P.: Upper Air Trough Axis Orientation and the Spatial-Distribution of Rainfall over Israel, Int. J. Climatol., 10, 57–62, 1990.

ACPD
11, 15659–15696, 2011

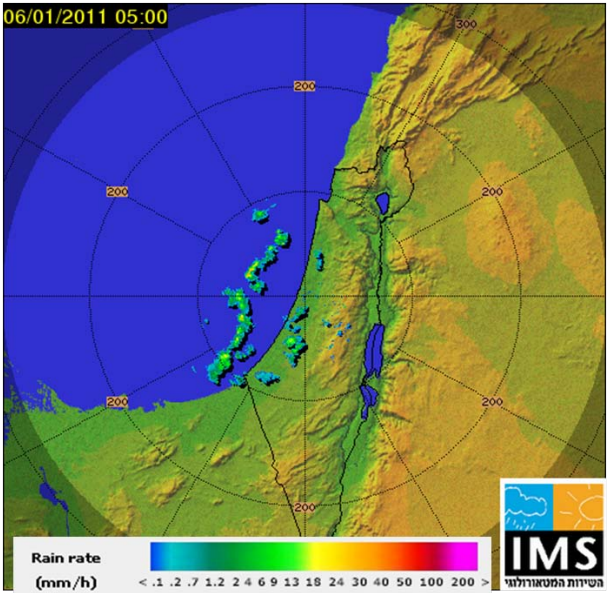

Fig. 1. Radar image of rain clouds off the coast of Israel, 6 January 2011 at 05:00 local time. The rain clouds in this approximate location dissipated a few hours after sunrise. The image serves as an example of a stationary precipitation line formed offshore, and is likely attributed to an offshore LB front. Image taken from the Israeli Meteorological Service (IMS) website, at http://www.ims.gov.il.

ACPD
11, 15659–15696, 2011

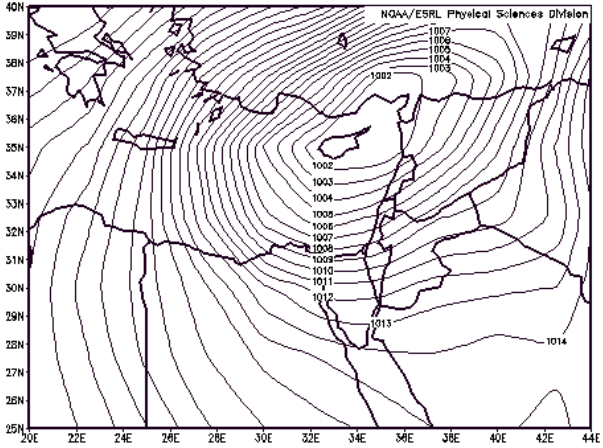

Fig. 2. Typical synoptic setting of Cyprus low in the EM, 29 January 2008. Mean sea level pressure isobars are displayed and labeled in hPa units. Image provided by the NOAA/OAR/ESRL PSD, Boulder, Colorado, USA, from their Web site at http://www.esrl.noaa.gov/psd/.

ACPD
11, 15659–15696, 2011

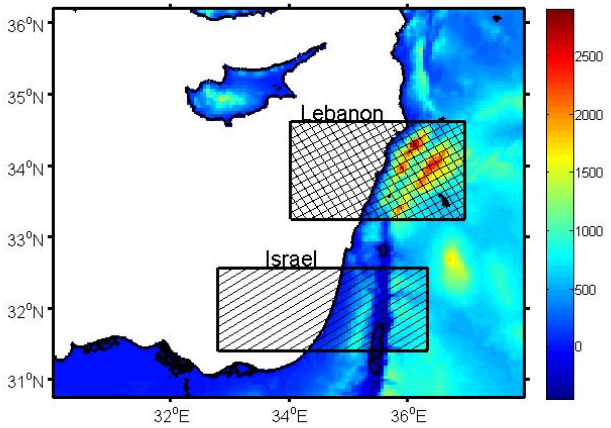

Fig. 3. Study area ROI and additional sub-regions. The colorbar represents topographic height above sea-level [m]. It should be noticed both that sub-regions include two successive mountain ranges nearly parallel to the coastline, but with Lebanon's mountains being higher and closer to the coast.

ACPD
11, 15659–15696, 2011

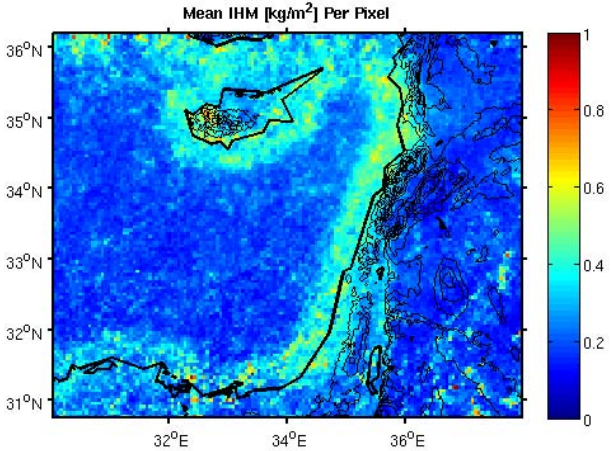

Fig. 4. Mean IHM [kg m^{-2}] per pixel, EM winter seasons 1998–2011. Black topography contours with vertical resolution of 300 m are added. A clear band of high IHM follows the EM coastlines.

ACPD
11, 15659–15696, 2011

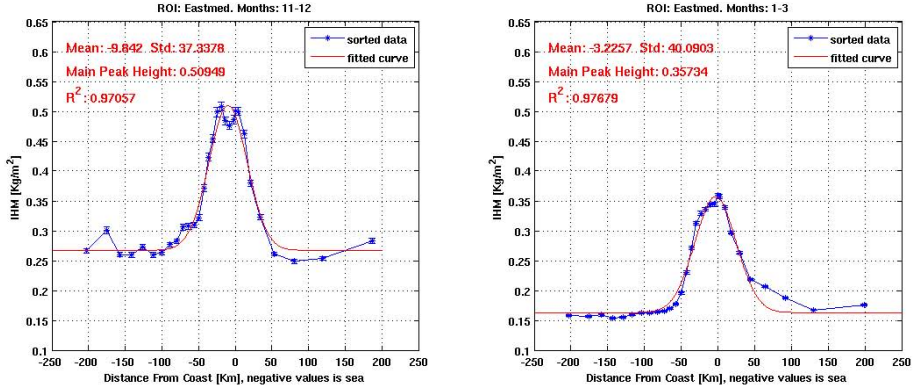

Fig. 5. Mean IHM [kg m^2] as a function of the distance from the nearest EM coastline, left figure corresponds to November–December months, and right figure to January–March. The data was sorted into 30 bins according to distance from nearest coastline and averaged (Blue astrix curve). A single Gaussian fit was applied to the sorted data curve (red curve), with the mean, standard deviation, peak height and correlation coefficient added in the upper left part of the figures. The November–December, January–March counts per bin are 11049, 20929, respectively.

ACPD
11, 15659–15696, 2011

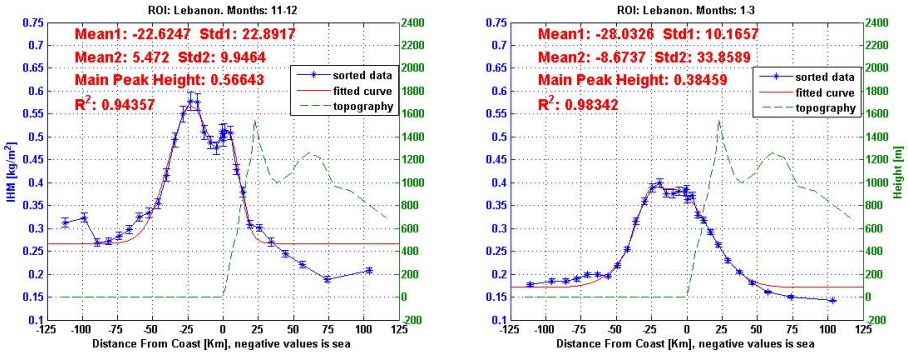

Fig. 6. Same as Fig. 5, but for "Lebanon" sub-region and with the addition of topography profile (dashed green curve) and superposition of multiple Gaussians. Gaussians are numbered from left to right, with #1 being the Gaussian peak which corresponds to LB mechanism. The two ridges reach their highest elevations at 21 km and 60 km inland. The November–December, January–March counts per bin are 2602, 4727, respectively.

ACPD
11, 15659–15696, 2011

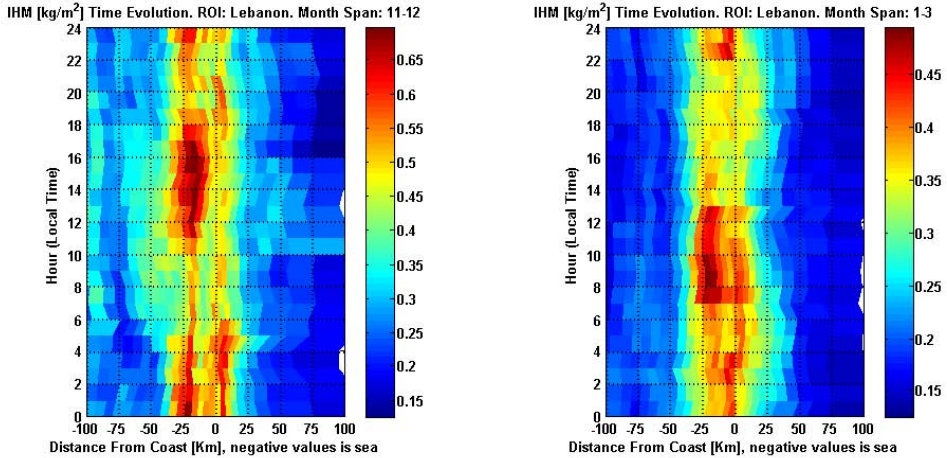

Fig. 7. Integrated Hydrometeor Mass time evolution with respect to coastline for November–December (left figure) and January–March (right figure), in the "Lebanon" sub-region. Colorbar scale represents IHM [kg m^{-2}], notice that colorbars are scaled differently for each sub-season in order to enhance the diurnal variance. Data was sorted as a function of distance from nearest coastline and local time. Y-axis numbers are the center local time of the ±3 h averaging time span, running from 00:00 (midnight) to 24:00. To interpret the Y-axis: 0–5 should be considered nighttime hours, 6–11 morning hours, 12–17 daytime hours and 18–23 evening hours. Pixel width reflects the density of counts, narrow pixels being denser. The November–December, January–March mean counts per bin are 647, 1176, respectively.

ACPD
11, 15659–15696, 2011

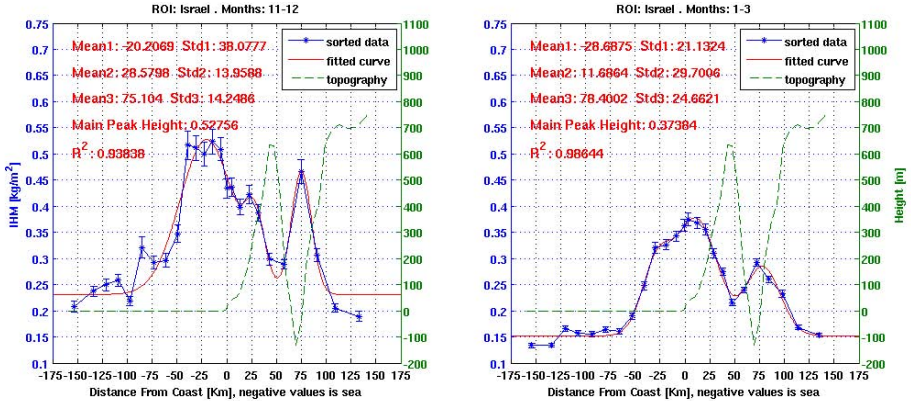

Fig. 8. Same as Fig. 6, but for "Israel" sub-region. Data was sorted into 25 bins. Judea and Jordan ridges reach their highest elevation at 46 km, 110 km respectively. The November–December, January–March counts per bin are 1072, 2139, respectively.

ACPD
11, 15659–15696, 2011

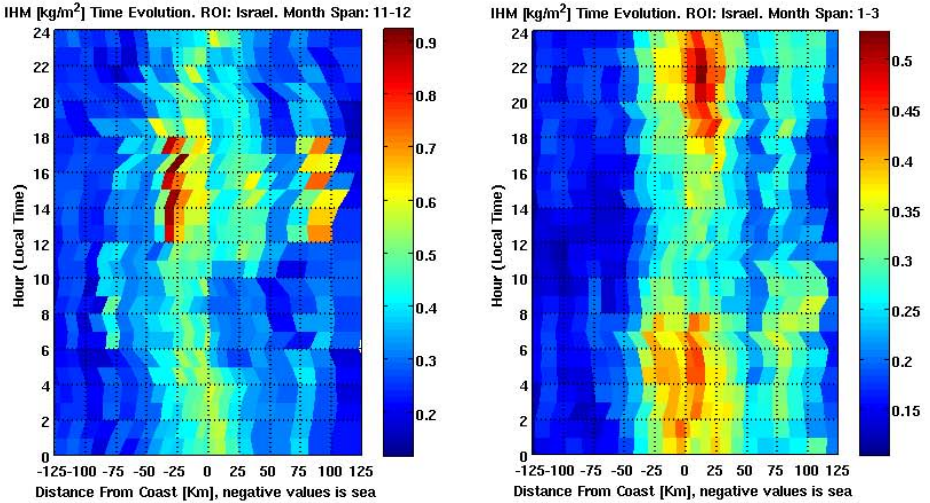

Fig. 9. Same as Fig. 7, but for "Israel" sub-region. Data was sorted into 25 bins. The November–December, January–March mean counts per bins are 269, 531, respectively.

ACPD
11, 15659–15696, 2011

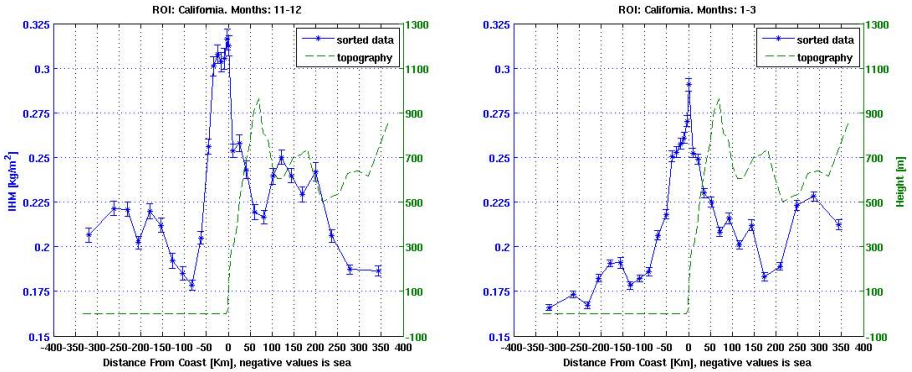

Fig. 10. Same as Fig. 6, but for Southern California (Lon: −125 to −117, Lat: 32 to 35.5) and without Gaussian fitting. The coast is followed by high topography that peaks around 65 km inland.

ACPD
11, 15659–15696, 2011